J Mater Sci (2008) 43:4135–4142
DOI 10.1007/s10853-007-2318-y

REES RAWLINGS FESTSCHRIFT

Effect of particle size on kinetics crystallization of an iron-rich glass

M. Romero · M. Kovacova · J. Ma. Rincón

Received: 13 July 2007 / Accepted: 13 November 2007 / Published online: 3 April 2008
© Springer Science+Business Media, LLC 2008

Abstract The effect of glass particle size on the crystallization kinetics of an iron-rich glass from a nickel leaching waste has been investigated by means of differential thermal analysis (DTA). The results show that the crystallization of a pyroxene phase occurs by bulk nucleation from a constant number of nuclei. The crystallization mode and the dimensionality of crystals are strongly dependent on the glass particle size, 100 μm being the critical size. Glass fractions with particle size >100 μm show three-dimensional crystal growth controlled by diffusion, whereas a particle size <100 μm leads to an interface reaction mechanism with two-dimensional growth of crystals.

Introduction

The term vitrification is commonly used to mean the process of converting a material into a glass-like amorphous solid, which is free from any crystalline structure. Glass-ceramics are ceramic materials formed through the controlled nucleation and crystallization of glass. Glass-ceramics were developed in the 1950s and find a wide variety of applications in different technological fields [1–5]. The earliest glass-ceramics were produced by a conventional glass route and subsequently crystallized, usually by heat treatment in two stages to give nucleation followed by crystal growth. In recent years, the sintering method has proven as a technically available route for glass-ceramics manufacture. This process usually involves milling a glass frit into fine particles, which are then shaped by conventional forming techniques and subsequently heat treated to provide sintering and crystallization of glass particles. Sintering process is normally used when the parent glass shows a strong tendency for surface crystallization or complex shapes are required.

Because glass and glass-ceramics are known to have many commercial applications, the transformation of wastes into glass or glass-ceramics provides the opportunity for making useful, marketable products out of wastes. Vitrification as a method of waste disposal was first applied in the 1970s to the immobilization of liquid high-level radioactive waste (HLW) [6, 7]. Since then, there has been a considerable research in this field, which concludes that vitrification process leads to a stable glass that is far superior in terms of durability, strength, and leach resistance compared to other waste stabilization technologies [8–12].

Glass ceramic method has also been used for the disposal of a wide diversity of non-nuclear inorganic wastes originating in both industrial and mining processes [13]. In this case, wastes are transformed into valuable products for subsequent use as ceramic floor tiles, abrasives or concrete additives. Among industrial wastes, special attention is paid to those with high iron oxide content, which leads to glass-ceramic materials characterized by high mechanical strength and good chemical stability. In last few years, iron-rich glass-ceramics have been obtained from zinc hydrometallurgy wastes [14–16], electric arc furnace dusts

---

M. Romero (✉) · J. Ma. Rincón
Group of Glassy and Ceramic Materials, Department of Building Construction Systems, Institute Eduardo Torroja for Construction Sciences-CSIC, C/ Serrano Galvache, 4, Madrid 28033, Spain
e-mail: mromero@ietcc.csic.es

M. Kovacova
Department of Physical and Physicochemical Mineral Processing Methods, Institute of Geotechnics, Slovak Academy of Sciences, Watsonova, 45, Kosice 04353, Slovak Republic

(EAFD) from the steel production [17–19], copper flotation wastes [20] and coal ashes [21].

Usually, inorganic wastes must be combined with glass-forming raw materials by heating a melt that then solidifies during cooling and gives rise to a glass. On occasions, batch compositions containing wastes lead to melts with a high tendency to crystallize during cooling, and the vitreous state can only be achieved through fast cooling by pouring the melt on water to obtain a frit. In these cases, glass-ceramics can be only prepared by sintering route, and the particle size of glass grains will play an important role in the crystallization process.

The aim of the present work is to determine the effect of glass particle size on the crystallization kinetics of an iron-rich glass produced by the melting of a nickel leaching residue (NLR) from hydrometallurgical nickel production.

Materials and methods

Raw materials used in the present investigation were a nickel leaching residue (NLR), glass cullet and dolomite. NLR is a waste coming from nickel production from Albanian laterite ore in a hydrometallurgical plant in Sereď (Slovakia). The annual production was around 3 × 10^5 tons, and since the end of production in 1993, close to 5.5 × 10^6 tons of waste remain at the dump. Even though the NLR contains more than 60 wt.% of iron in oxide form, it is not suitable as feed for steelmaking industry because of its high content of chromium. Table 1 shows the chemical composition of raw materials as determined by atomic absorption spectroscopy (AAS). Iron oxide is the main component in NLR, which also shows a low content of both glass-forming (SiO_2) and stabilizing oxides (alkaline earth oxides). For this reason, glass cullet and dolomite have been used in the formulation of NLR glass, which was prepared by mixing 30% NLR, 60% glass cullet and 10% dolomite. Homogenized batches were placed in alumina-silica crucibles and heated at 15 °C/min in a high-temperature electric furnace up to 1450 °C. After a holding time of 30 min, the melt was quenched by pouring into water.

Table 1 Chemical analysis (wt.%) of raw materials determined by AAS

Oxide	NLR	Glass cullet	Dolomite
SiO_2	15.03	72.4	0.59
Al_2O_3	4.80	1.7	0.34
CaO	3.54	9.6	29.61
MgO	2.21	1.7	22.47
Fe_2O_3	38.57	0.05	0.29
FeO	22.64	–	–
Na_2O	–	13.8	0.04
K_2O	–	0.6	0.11
Cr_2O_3	1.06	–	–
NiO	0.17	–	–
LOI	11.98	–	46.35

To investigate the effect of particle size on crystallization kinetics of NLR glass, the frit was separated by sieving in six fractions with different particle size ranges as shown in Table 2.

The vitreous or crystalline state of NRL glass before and after thermal treatment was established by X-ray diffractometry. Samples were crushed to fine powder in an agate mortar, passed through a 300-mesh sieve and then scanned with CuKα radiation from $3° \leq 2\theta \leq 60°$ at a scanning speed of 0.5°/min, using a Philips X'PERT MPD diffractometer operating at 30 mA and 50 kV.

Differential thermal analysis (DTA/TG) was performed on NLR glass fractions in a SETARAM Labsys Thermal Analyser. The samples were heated from room temperature to 1250 °C at heating rates of 5, 10, 15, 25, 40 and 50 °C/min. The DTA scans were conducted in flowing air using platinum crucibles with calcined Al_2O_3 as reference material. All the DTA curves were normalized with respect to the sample weight.

The analysis of crystallization kinetics has been accomplished from DTA curves on the basis of the Johnson-Mehl-Avrami (JMA) theory, which describes the evolution of the crystallization fraction, x, with time, t, during a phase transformation under an isothermal condition.

$$x = 1 - \exp\left[-(kt)^n\right] \tag{1}$$

where x is the volume fraction crystallized after time t, n the Avrami exponent and k the reaction rate constant, whose temperature dependence is generally expressed by the Arrhenian-type equation:

$$k = k_0 \exp\left(-E/\mathrm{RT}\right) \tag{2}$$

where k_0 is the frequency factor, E is the apparent activation energy, R is the ideal gas constant and T is the isothermal temperature in Kelvin.

The crystallization rate can be expressed by:

$$\frac{\mathrm{d}x}{\mathrm{d}t} = kf(x) = k_0 \exp\left(-\frac{E}{\mathrm{RT}}\right)f(x) \tag{3}$$

and taking logarithms,

Table 2 Particle size ranges separated by sieving from NLR frit

Fraction	Particle size range (μm)
*f*1	400–500
*f*2	250–400
*f*3	100–250
*f*4	80–100
*f*5	63–80
*f*6	<63

$$\ln\left(\frac{\mathrm{d}x}{\mathrm{d}t}\right) = \ln\left[k_0 f(x)\right] - \frac{E}{\mathrm{RT}} \tag{4}$$

These equations have been derived for isothermal crystallization process, but they can be applied with certain restrictions to non-isothermal experiments with satisfactory results [22].

During a phase transformation under an isothermal condition the crystallization fraction, x, at a temperature T differs at different heating rates and, hence, the curves of dx/dt versus temperature are also different. In this case, the crystallization kinetic can be studied by the mathematical method proposed by Ligero et al. [23], which has been effectively applied for interpreting DTA results from different materials [24–26]. If we select the same value of x in every experiment at different heating rates, there should be a linear relationship between the corresponding dx/dt and 1/T, whose slope gives the activation energy, E. Then, it is possible to calculate, through Eq. 4, the value of ln[k_0 $f(x)$] for each crystallized fraction at each heating rate. From the plot of ln[k_0 $f(x)$] versus x, we can select many pairs of x_1 and x_2 that satisfied the condition

$$\ln\left[k_0 f(x_1)\right] = \ln\left[k_0 f(x_2)\right] \tag{5}$$

and therefore,

$$\begin{aligned}\ln(1-x_1) + \frac{n-1}{n}\ln\left[-\ln(1-x_1)\right] \\ = \ln(1-x_2) + \frac{n-1}{n}\ln\left[-\ln(1-x_2)\right]\end{aligned} \tag{6}$$

and the Avrami parameter, n, can be calculated by,

$$n = \ln\left[\ln(1-x_2)/\ln(1-x_1)\right]/\ln\left[\frac{(1-x_2)\ln(1-x_2)}{(1-x_1)\ln(1-x_1)}\right] \tag{7}$$

Once the Avrami parameter is determined, the frequency factor, k_0, can also be calculated by equation:

$$\begin{aligned}\ln\left[k_0 f(x)\right] = \ln k_0 + \ln n + \ln(1-x) \\ + \frac{n-1}{n}\ln\left[-\ln(1-x)\right]\end{aligned} \tag{8}$$

The Avrami parameter, n, indicates the crystallization mode. Another useful parameter is the numerical factor, m, which depends on the dimensionality of crystal growth and is derived from the Matusita and Sakka equation for non-isothermal DTA experiments [27–29]:

$$\ln\left(\frac{\phi^n}{T_p^2}\right) = -\frac{mE}{\mathrm{RT}_p} + \mathrm{const} \tag{9}$$

where ϕ is the heating rate and T_p is the temperature at the maximum of crystallization peak.

Results and discussion

The glassy nature of the as-quenched frit is established by XRD in Fig. 1, which depicts the typical amorphous halo characteristic of glassy materials. Table 3 shows the chemical analysis of NLR glass by XRF, SiO_2, Fe_2O_3 and CaO being the major components. Compared to other silicate glasses, NLR glass is distinguished by a high iron oxide content, which will confer a high crystallization tendency to the glass. In fact, this composition can be only achieved in a glassy state by means of fast cooling by pouring the melt on water.

Figure 2 shows representative DTA curve recorded on 80–100 μm fraction during heating from room temperature to 1250 °C at a heating rate of 25 °C min^{-1}. The glass shows the glass transition, T_g, at 610 °C followed by the only exothermic crystallization peak, T_p, in the 755–783 °C range. Finally, an endothermic reaction at 1035 °C indicates formation of a liquid phase. The exothermic peak is due to the crystallization of a pyroxene phase from the diopside-hedenbergite group, which forms a completed solid-solution series between $CaMgSi_2O_6$ (diopside) and $CaFeSi_2O_6$ (hedenbergite) [30], as has been identified by XRD analysis on NLR glass sintered at 750 °C for 30 min (Fig. 1). Pyroxene-type phases are typical phases precipitated in glass-ceramics from iron-rich wastes, in which crystallization occurs through liquid–liquid immiscibility, where one of the liquid phases is richer in iron and

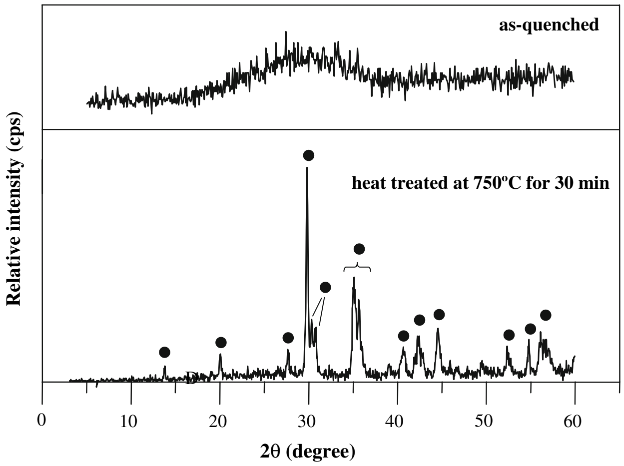

Fig. 1 XRD patterns of NLR glass frit as-quenched and after heat treatment at 750 °C during 30 min (● = pyroxene phase from the diopside-hedenbergite series)

Table 3 Chemical analysis (wt.%) of NLR glass as determined by XRF

SiO_2	Al_2O_3	Fe_2O_3	CaO	MgO	Na_2O	K_2O	TiO_2	Cr_2O_3
48.07	3.59	22.34	11.79	4.62	7.77	0.66	0.09	1.06

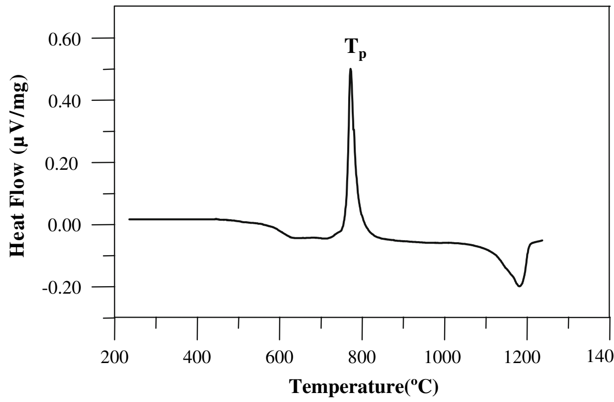

Fig. 2 DTA curve from *f*4 fraction (80–100 µm) heated at 25 °C min^{-1}

promotes a spontaneous formation of the magnetite spinels nano-crystals, which act as nuclei for the formation of the main pyroxene phase [31, 32].

Figure 3 depicts the DTA curves recorded on different particle size fractions of NLR glass at a heating rate of 25 °C. The temperature of the maximum of the exothermic peak, T_p, shifts to a higher temperature as the particle size decreases from 500 to <63 µm. In addition, the height and the width of crystallization peak are also changing. Thus, Fig. 3 indicates that the crystallization kinetics of NLR glass will be highly subject to the glass particle size.

As is usual in glasses, if we consider a specific particle size fraction, the temperature of the maximum of the exothermic peak, T_c, shifts to higher temperatures as the heating rate increases. For instance, Fig. 4 depicts the DTA curves recorded on the 80–100 µm fraction at different heating rates. From each of those curves, the crystallization fraction, x, can be determined by the ratio:

$$x = \frac{A_T}{A},$$

where A_T is the area of the exothermic peak in the DTA curve at temperature T, and A is the total area under the peak.

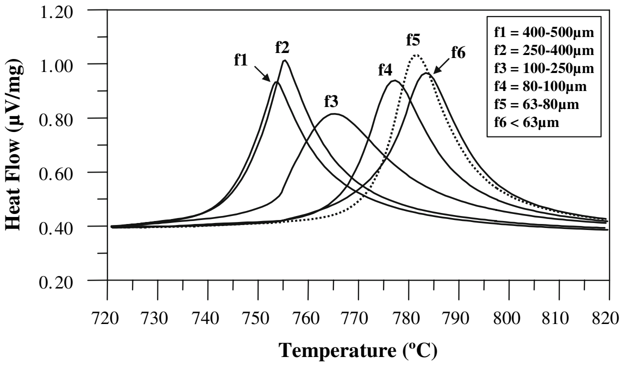

Fig. 3 DTA curves for different particle size fractions of NLR glass at a heating rate of 25 °C

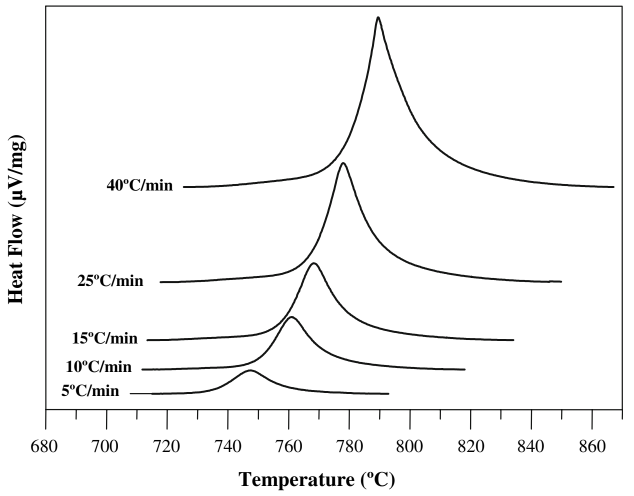

Fig. 4 DTA curves from *f*4 fraction (80–100 µm) at different heating rates

Figure 5 represents the variations of x with temperature for the 80–100 µm fraction under different heating rates. As presumed from the different sizes of curves in Fig. 4, the crystallization fraction at a fixed temperature varies with heating rates and, consequently, the representations of dx/dt versus time are also different as shown in Fig. 6, which depicts the growth rate of pyroxene phase with time for different heating rates. As expected, the rate of crystallization increases with the heating rate.

Figure 7 depicts the plot of ln(dx/dt) versus 1/T at the same value of crystallized fraction from the experiment carried out on *f*4 fraction (80–100 µm) at different heating rates. Analogous curves are obtained for the different particle size fractions. For each fraction, it is possible to select a crystallized fraction range for which ln(dx/dt) fits a straight line with the absolute temperature inverse. The activation energy, E, can be then determined from the slope of those lines. The values of E calculated the different crystallized fractions and the average values for the different particle size fractions are listed in Table 4. For

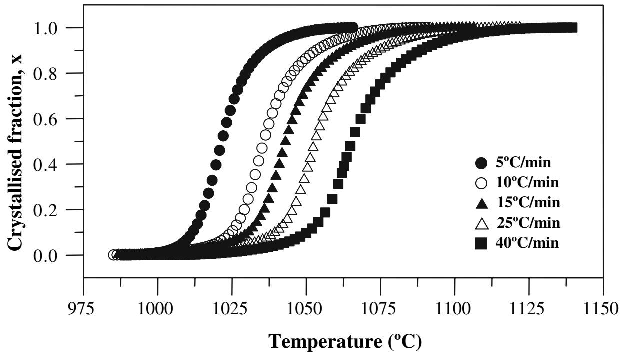

Fig. 5 Variation of crystallized fraction with temperature for *f*4 fraction (80–100 µm) under different heating rates

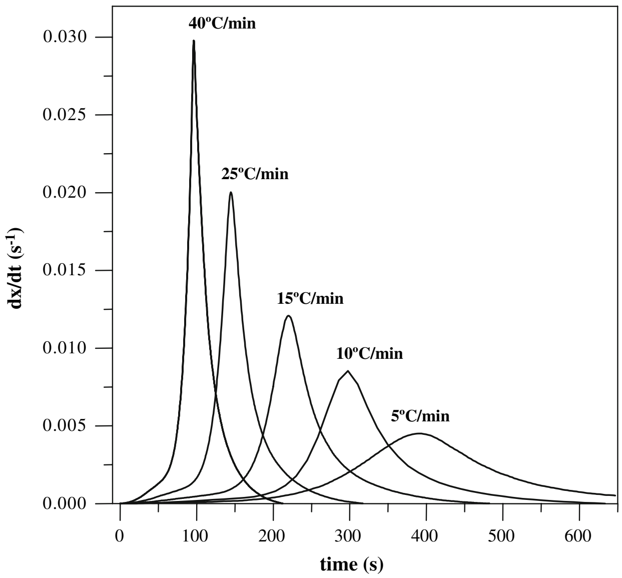

Fig. 6 Growth rate of pyroxene phase with time for *f*4 fraction (80–100 μm) at different heating rates

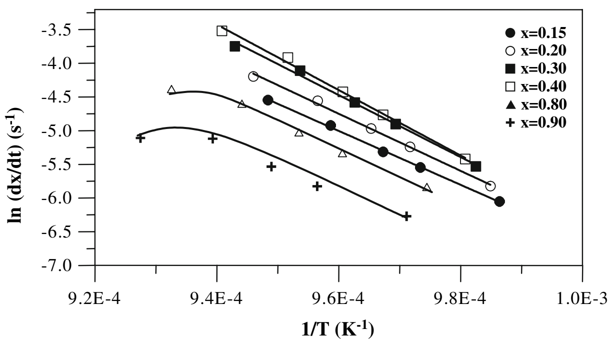

Fig. 7 Plot of ln(d*x*/d*t*) versus 1/*T* at the same value of crystallized fraction from the experiment carried out on *f*4 fraction (80–100 μm) at different heating rates

calculations, only values of crystallized fraction that lead to highly reliable fitting (coefficient of determination, $r > 0.99$) have been taken into account. The average activation energy of pyroxene-phase devitrification for the different particle size fractions is shown in Fig. 8. It can be seen that the fractions can be sorted out in two groups with 100 μm as the critical particle size. This result indicates that the crystallization in NLR glass occurs by different mechanisms depending on the glass particle size. This fact will be explained afterwards.

The value of $\ln[k_0\ f(x)]$ for the different particle size fractions can be calculated once their activation energy is known and the Avrami parameter, *n*, is determined by selecting several pairs of x_1 and x_2 that satisfy the condition $\ln[k_0\ f(x_1)] = \ln[k_0\ f(x_2)]$. Figure 9 shows the plot of

Table 4 Values of E calculated for the different particle size fractions

Particle size	Crystallized fraction	*r*	E_x (kJ mol^{-1})	*E* (kJ mol^{-1})
<63 μm	$x = 0.12$	0.989	–	386
	$x = 0.13$	0.992	366	
	$x = 0.15$	0.995	368	
	x = 0.20	0.997	377	
	$x = 0.30$	0.997	393	
	$x = 0.40$	0.993	407	
	$x = 0.41$	0.991	405	
	$x = 0.42$	0.988	–	
63–80 μm	$x = 0.10$	0.986	–	365
	$x = 0.11$	0.996	363	
	$x = 0.12$	0.993	357	
	$x = 0.15$	0.992	366	
	$x = 0.17$	0.991	370	
	$x = 0.18$	0.992	368	
	$x = 0.19$	0.987	–	
80–100 μm	$x = 0.10$	0.991	325	351
	$x = 0.12$	0.996	333	
	$x = 0.15$	0.999	343	
	$x = 0.20$	0.997	352	
	$x = 0.30$	0.995	372	
	$x = 0.40$	0.996	384	
	$x = 0.45$	0.991	374	
	$x = 0.46$	0.898	–	
100–250 μm	$x = 0.10$	0.999	422	423
	$x = 0.20$	0.998	417	
	$x = 0.30$	0.998	420	
	$x = 0.40$	0.997	429	
	$x = 0.50$	0.996	428	
	$x = 0.60$	0.994	422	
	$x = 0.63$	0.898	–	
250–400 μm	$x = 0.10$	0.996	356	370
	$x = 0.15$	0.996	352	
	$x = 0.20$	0.994	358	
	$x = 0.25$	0.994	372	
	$x = 0.30$	0.994	389	
	$x = 0.32$	0.992	395	
	$x = 0.33$	0.989	–	
400–500 μm	$x = 0.10$	0.995	353	349
	$x = 0.11$	0.996	342	
	$x = 0.13$	0.992	344	
	$x = 0.15$	0.991	349	
	$x = 0.17$	0.991	351	
	$x = 0.18$	0.991	354	
	$x = 0.19$	0.987	–	

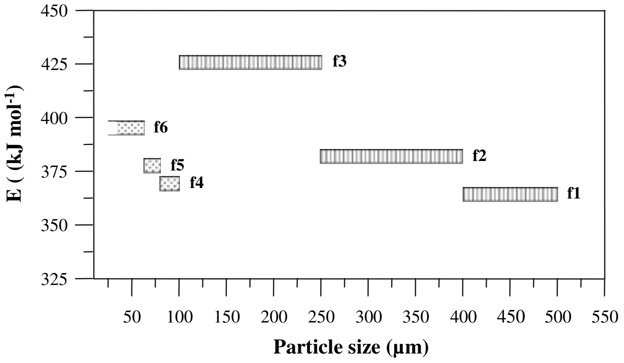

Fig. 8 Average activation energy of pyroxene phase devitrification for the different particle size fractions

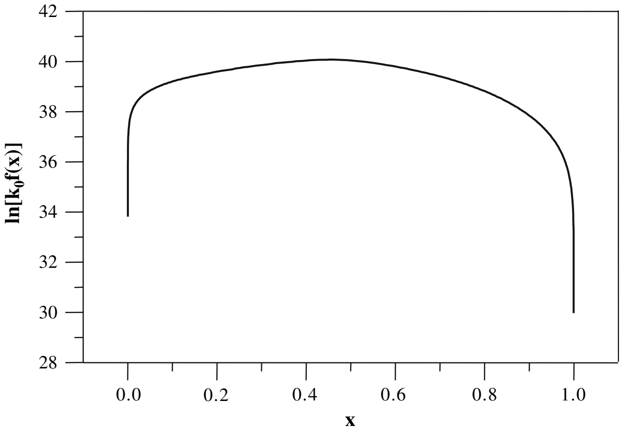

Fig. 9 Plot of ln[k_0 $f(x)$] versus crystallization fraction for 80–100 µm fraction heated at 25 °C min^{-1}

Table 5 Values of n calculated for the different particle size fractions

Particle size (µm)	Heating rate (°C min^{-1})	n_ϕ	n	$k_{0,\phi}$ (s^{-1})	k_0 (s^{-1})
<63	5	1.75	1.65 ± 0.06	1.34×10^{17}	1.29×10^{17}
	10	1.63		1.39×10^{17}	
	15	1.57		1.17×10^{17}	
	25	1.63		1.69×10^{17}	
	40	1.67		8.64×10^{16}	
63–80	5	1.65	1.56 ± 0.05	1.09×10^{16}	9.79×10^{15}
	10	1.56		9.40×10^{15}	
	15	1.53		8.99×10^{15}	
	25	1.56		1.04×10^{16}	
	40	1.53		9.25×10^{15}	
80–100	5	1.68	1.57 ± 0.08	4.31×10^{15}	3.72×10^{15}
	10	1.65		3.59×10^{15}	
	15	1.53		3.49×10^{15}	
	25	1.50		3.73×10^{15}	
	40	1.49		3.49×10^{15}	
100–250	5	1.47	1.40 ± 0.05	1.55×10^{19}	1.40×10^{19}
	10	1.44		1.52×10^{19}	
	15	1.42		1.43×10^{19}	
	25	1.34		1.26×10^{19}	
	40	1.36		1.23×10^{19}	
250–400	5	1.46	1.45 ± 0.05	4.84×10^{16}	5.21×10^{16}
	10	1.49		5.78×10^{16}	
	15	1.50		6.65×10^{16}	
	25	1.43		4.92×10^{16}	
	40	1.38		3.87×10^{16}	
400–500	5	1.60	1.49 ± 0.08	5.32×10^{15}	5.45×10^{15}
	10	1.40		7.80×10^{15}	
	15	1.43		5.25×10^{15}	
	25	1.45		4.98×10^{15}	
	40	1.47		3.90×10^{15}	

ln[k_0 $f(x)$] versus crystallization fraction for 80–100 µm fraction heated at 25 °C min^{-1}. Similar curves are obtained for the different heating rates and particle size fractions. Table 5 shows the calculated values at different heating rates and the average values of Avrami parameter, n, and the frequency factor, k_0. It can be seen that there is a strong increase in the magnitude of k_0 from 80–100 µm fraction ($k_0 = 3.72 \times 10^{15}$ s^{-1}) to 100–250 µm fraction ($k_0 = 1.4 \times 10^{19}$ s^{-1}). As the frequency factor is related to the vibration frequency of atoms in the crystal-liquid interface [33], the observed change indicates a strong viscosity variation just around the critical particle size (100 µm).

Figure 10 shows the fitting of Matusita Eq. 9 for the different particle size fractions. Once the values of n and E are known, the slope of the lines yields the m factor.

Figure 11 depicts the location of $f1$–$f6$ fractions regarding their values of n and m compared to different crystallization mechanisms according to Matusita et al. [34]. All fractions are located on the region of bulk nucleation mechanism with constant number of nuclei. However, it can be seen that in agreement with Fig. 8, the fractions are arranged in two groups. Both the parameters n and m are both close to 1.5 in fractions with particle size >100 µm, which is an indication, according to Matusita, of a diffusion-controlled mechanism with three-dimensional growth of pyroxene crystals with polyhedron-like morphology. As for finer fractions with particle size <100 µm, n and m parameters are shifted to values close to 2, which indicates an interface reaction mechanism with two-dimensional growth of pyroxene crystals with plates-like morphology. The values of n for $f1$–$f6$ fractions are in the 1.40–1.65 interval, which is in agreement with values of n in the 1.2–1.8 interval previously reported for iron-rich glasses [16, 21, 32]. As for m parameter, there is a lack in the literature of the determination of such parameter and, hence it was not possible to evaluate against similar glasses.

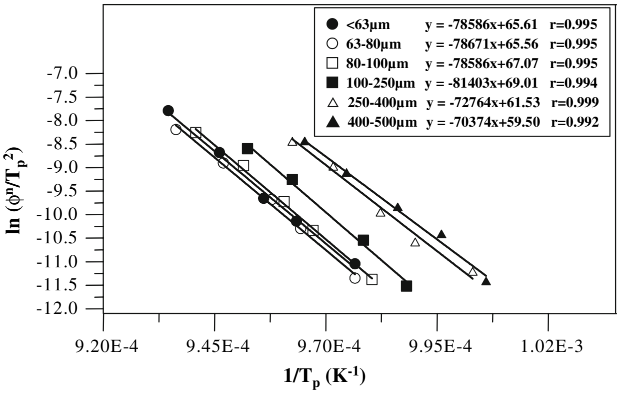

Fig. 10 Fitting of Matusita equation for the different particle size fractions

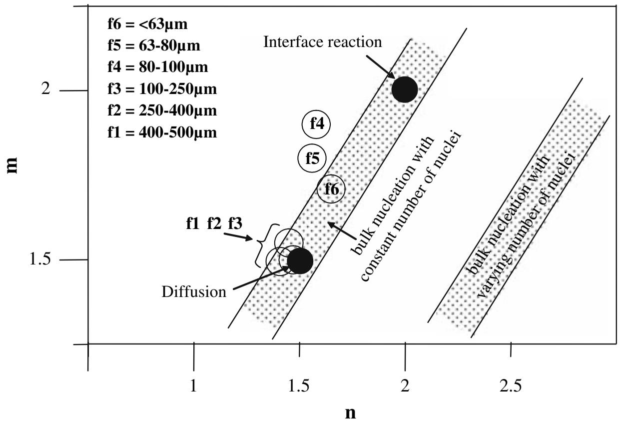

Fig. 11 Plot of *n* and *m* parameters for *f*1–*f*6 fractions comparing to different crystallization mechanisms according to Matusita et al. [34]

Conclusions

The effect of particle size on crystallization kinetics and growth mechanism of an iron-rich glass produced by melting a waste coming from nickel hydrometallurgical production have been investigated by DTA method on a glass prepared by mixing 30% waste, 60% glass cullet and 10% dolomite. From the experimental results the following conclusions can be drawn:

- The temperature of the maximum of the exothermic peak shifts to higher temperatures as the particle size decreases from 500 to <63 µm.
- The average activation energy, *E*, of pyroxene-phase devitrification for the different particle size fractions is in the 349–423 kJ mol^{-1} interval. The arrangement of *E* with particle size indicates that crystallization in the glass occurs by different mechanisms depending on the glass particle size, 100 µm being the critical particle size.
- The values of the calculated growth morphology parameters, *n* and m, indicate that bulk nucleation from a constant number of nuclei is the dominant mechanism for pyroxene crystallization.
- Glass fractions with particle size >100 µm show values of *n* and *m* parameters close to 1.5, indicating a three-dimensional growth of crystals with polyhedron-like morphology.
- Glass fractions with particle size <100 µm show values of *n* and *m* parameters near 2, indicating an interface reaction mechanism with two-dimensional growth of crystals with plates-like morphology.
- The values of the frequency factor, k_0, are in the 3.72×10^{15}–1.40×10^{19} s^{-1}range and show a strong change around the critical particle size.

Acknowledgement This investigation has been carried out in the frame of a co-operation project between the Spanish Council for Scientific Research (CSIC) and the Slovak Academy of Sciences (SAS).

References

1. Partridge G (1994) Glass Technol 35:116
2. Partridge G (1994) Glass Technol 35:171
3. James PF (1995) J Non-Cryst Solids 181:1
4. Pannhorst W (1997) J Non-Cryst Solids 219:198
5. Höland W, Beall G (2002) In: Glass-ceramic technology. The American Ceramic Society, Ohio
6. Bocola W, Donato A (1972) Energia Nucleare 19(6):390
7. Donato A, Bocola W (1972) Energia Nucleare 19(7):459
8. Hidalgo M, Rincón JMA (1987) Bol Soc Esp Ceram Vidr 26:227
9. Donald IW, Metcalfe BL, Taylor RNJ (1997) J Mater Sci 32:5851. doi:10.1023/A:1018646507438
10. Hrma P, Crum JV, Bates DJ, Bredt PR, Greenwood LR, Smith HD (2005) J Nucl Mater 345(1):19
11. Hrma P, Crum JV, Bredt PR, Greenwood LR, Arey BW, Smith HD (2005) J Nucl Mater 345(1):31
12. Kaushik CP, Mishra RK, Sengupta P, Kumar A, Das D, Kale GB, Raj K (2006) J Nucl Mater 358(2–3):129
13. Rawlings RD, Wu P, Boccaccini AR (2006) J Mater Sci 41(3):733. doi:10.1007/s10853-006-6554-3
14. Romero M, Rincón JMA (1999) J Am Ceram Soc 82:1313
15. Karamanov A, Taglieri G, Pelino M (1999) J Am Ceram Soc 82:3012
16. Karamanov A, Pisciella P, Pelino M (2000) J Eur Ceram Soc 20:2233
17. Kavouras P, Loannidis TA, Kehagias T, Tsilika I, Chrissafis K, Kokkou S, Zouboulis A, Karakostas T (2007) J Eur Ceram Soc 27(5):2317
18. Kavouras P, Kehagias T, Tsilika I, Kaimakamis G, Chrissafis K, Kokkou S, Papadopoulos D, Karakostas T (2007) J Hazard Mater 139(3):424
19. Pelino M, Karamanov A, Pisciella P, Crisucci S, Zonetti D (2002) Waste Manage 22(8):945
20. Karamanov A, Aloisi M, Pelino M (2007) J Hazard Mater 140(1–2):333
21. Francis AA, Rawlings RD, Sweeney R, Boccaccini AR (2004) J Non-Cryst Solids 333:187
22. Surinach S, Baro MD, Clavaguera MT, Clavaguera N (1983) J Non-Cryst Solids 58:209
23. Ligero RA, Vazques J, Casas-Ruiz M, Jiménez-Garay RA (1991) J Mater Sci 26:211. doi:10.1007/BF00576054

24. Campos AL, Silva NT, Melo FCL, Oliveira MAS, Thim GP (2002) J Non-Cryst Solids 304:9
25. Wei P, Rongti L (1999) Mater Sci Eng A 271:298
26. Romero M, Martín-Márquez J, Rincón JMA (2006) J Eur Ceram Soc 26:1647
27. Matusita K, Sakka S, Matsui Y (1975) J Mater Sci 10:961. doi: 10.1007/BF00823212
28. Matusita K, Sakka S (1979) Phys Chem Glasses 20:81
29. Matusita K, Sakka S (1980) J Non-Cryst Solids 38–39:741
30. Deer WA, Howie RA, Zussman J (1992) In: The rock-forming minerals. Pearson Education Limited, Essex, p 170
31. Romero M, Rincon JMA (1998) J Eur Ceram Soc 18:153
32. Karamanov A, Pelino M (2001) J Non-Cryst Solids 281:139
33. Rincón JMA (1992) Polym Plast Technol Eng 31:309
34. Matusita K, Miura K, Komatsu T (1985) Thermochim Acta 88:283